PCCP

ROYAL SOCIETY OF CHEMISTRY

PAPER

View Article Online
View Journal

Check for updates

Cite this: DOI: 10.1039/d4cp02754j

Hollow titanium nitride nanoshells for enhanced plasmon-driven hot electron generation and improved photocatalytic and photovoltaic applications

Samar Moustafa,*[ab] Mohamed K. Zayed,[bc] K. O. Daffallah,[bd] Nagih M. Shaalan,[ae] Mohamed Rashad[af] and Hesham Fares[ab]

Nowadays, plasmonic titanium nitride (TiN) is widely employed as a potential alternative to noble metals in semiconductor–metal hybrid nanoparticles (S–M HNPs) for improving the utilization efficiency of solar energy in photocatalytic and photovoltaic systems. In semiconductor–TiN nanosystems, TiN NPs convert solar energy into highly energetic (hot) electrons that can be transmitted to the attached semiconductor for enhanced applications. In this paper, we propose TiN nanoshells with a nonabsorbing dielectric core as an improved energy conversion component in S–M HNPs, compared to homogenous TiN nanospheres, with higher geometrical optimization flexibility, wider absorption range tuneability, and effective hot electron generation and utilization due to the reduced plasmonic-shell size. For understanding the impact of the core material on the functionality of the nanoshells, we assume three core materials with different refractive indices (air, silica (SiO_2), and magnesium oxide (MgO)). The exact Mie theory is utilized to calculate the absorption coefficient and the plasmon field of the proposed TiN nanoshells. To quantify the absorbance effectiveness on the solar spectrum, we calculate a relevant figure of merit (FoM) that depends on the spectral features of the absorption coefficient. By optimizing the geometrical parameters of nanoshells, it is found that hollow TiN nanoshells with the lowest core refractive index exhibit the highest FoM of solar energy absorption. Also, the plasmon field intensity of hollow TiN nanoshells is higher and more concentrated in a smaller volume of TiN material in comparison to the field intensity of other nanoshells (SiO_2–TiN and MgO–TiN nanoshells) and TiN nanospheres. Factors affecting the utilization of the generated hot electrons, including the radiative damping of plasmons and the spreading of the plasmon field inside the nanoparticles, have been investigated. In view of the temporal dynamics of hot electrons, it is shown that using the hollow TiN nanoshells with thin shells greatly enhances the effectiveness of the generated hot electrons to reach the attached semiconductor. In fact, the reduced plasmonic-shell thickness results in a trade-off between a longer radiative relaxation time and less solar energy absorption with regard to the selected core material.

Received 11th July 2024,
Accepted 26th September 2024

DOI: 10.1039/d4cp02754j

rsc.li/pccp

1. Introduction

Localized surface plasmon resonance (LSPR), a collective oscillation of electrons at the surface of plasmonic nanoparticles (NPs) excited by in-phase incident light, is one of the hottest fields of research in photocatalysis and solar energy conversion. However, the enhancement of photochemical reactions through photogenerated electrons and holes in semiconductor catalysts by sunlight absorption exhibits a very low efficiency of solar–chemical energy conversion (5–10%).[1] Thanks to its excellent stability, low cost, and environmental friendliness, TiO_2 is the most traditional semiconductor photocatalyst.[2,3] The relatively wide bandgap of TiO_2 ($\sim$3.2 eV for anatase TiO_2[4]) imposes a significant limitation on its photocatalytic activity where it can only be triggered by UV light with photon energies in the range of 3–124 eV (100–400 nm). In the so-called semiconductor–metal hybrid nanoparticles (S–M HNPs),[5] noble metal NPs are attached to the surface of a semiconductor, commonly TiO_2, allowing harvesting of solar radiation in the visible and near-infrared (NIR) ranges. The use of S–M HNPs improves the efficiency of

---

[a] Department of Physics, Faculty of Science, Assiut University, Assiut 71516, Egypt. E-mail: sabdelraheem@taibahu.edu.sa
[b] Physics Department, College of Science, Taibah University, P. O. Box 30002, Madinah, Saudi Arabia
[c] Physics Department, Faculty of Science, Beni-Suef University, Beni-Suef, 6111, Egypt
[d] Electronic Engineering Department, Faculty of Engineering and Technology, University of Gezira, P.O. Box 20, Wadmedani, Sudan
[e] Department of Physics, College of Science, King Faisal University, P.O. Box 400 Al-Ahsa 31982, Saudi Arabia
[f] Physics Department, Faculty of Science, University of Tabuk, Tabuk 71491, Saudi Arabia

the photocatalytic and photovoltaic processes through two mechanisms. The first mechanism is ascribed to the inhibition of the electron–hole recombination by the Schottky barrier formed at the metal–semiconductor interface.[6] The second is the production of highly energetic (hot) electrons and holes due to the nonradiative decay of surface plasmons. These hot electrons transfer from the plasmonic metal (co-catalyst) to the low-energy conduction band of the semiconductor (catalyst), leading to charge separation.[7] The use of plasmon assisted hot electron generation in S–M HNPs, particularly the Au/TiO_2 system, has been demonstrated as a viable technique to improve the solar cells' efficiency and hydrogen production rate in the photoelectrochemical water splitting process.[8,9]

In S–M HNPs, noble metal co-catalysts present a number of obstacles to their use in photothermal energy conversion applications, including their inadequate narrow-band absorption of solar radiation, high conversion to thermal energy, thermal instability, complementary metal–oxide–semiconductor (CMOS) incompatibility, and high cost. Aluminum nanocrystals have been proposed as possible plasmonic photocatalysts that can generate hot electrons effectively and affordably.[10,11] The high reactivity with air and water and poor thermal stability at high local temperatures are the main obstacles that hinder the practical implementation of Al NPs in large-scale plasmonic-assisted photocatalytic applications. Transition metal nitrides (TMNs) have recently emerged as excellent alternative plasmonic materials for transforming solar energy into energetic electrons that can be stored in chemical bonds for use in photocatalytic reactions or to improve the performance of photovoltaic cells. Of all the TMN materials, TiN is especially favored due to its broadband high absorption cross-section across the solar spectrum.[12] TiN outperforms noble metals in terms of cost, compatibility with CMOS technology, mechanical strength and durability, and chemical and thermal stability (*i.e.*, a melting point of $\sim$2930 °C). However, the high tendency of TiN NPs to convert solar radiation to heat is a serious drawback that reduces the efficiency of solar energy conversion to charge carriers.[13] By attaching TiN NPs to most semiconductor metal oxides (SMOs) (*e.g.*, TiO_2), a Schottky barrier with a very small height (almost an ohmic junction) is formed at the TiN–SMO interface. For instance, the Schottky barrier at the TiN/TiO_2 interface is only about 0.1 eV.[14] This energy band alignment in the TiN–SMO system allows for high photocurrent due to both cold and hot electron excitation. In experiments,[15] the TiN/TiO_2 hybrid structure has been shown to yield a 25% higher photocurrent than the Au/TiO_2 hybrid structure. In addition, the potential use of TiN NPs as a cost-effective alternative to Au and Ag NPs in plasmon-driven chemical activities has been previously confirmed *via* photoreduction of platinum ions under visible-NIR illumination.[16] In a previous study,[17] TiN NPs with controllable size ($<$10 nm), narrow size distribution, high throughput, good structural quality, and composition-tunable plasmonic resonance ($\sim$800 nm to 1000 nm) have been effectively synthesized using a continuous flow non-thermal plasma process. Other numerous experimental studies have been conducted using different synthesis techniques for improving the structural characteristics and plasmon resonance response of TiN NPs, which is an essential step for their successful utilization in various plasmonic-based applications.[18,19]

The LSPR field is normally decayed due to three crucial loss channels, radiative decay in the form of spontaneous emission, and non-radiative decay by interband excitations (hot electrons) and intraband excitations of single electrons.[20,21] The LSPR wavelength of NPs is influenced by the size, shape, structure, and material of plasmonic NPs as well as the dielectric function of the surrounding medium. By controlling these factors, the LSPR wavelength can be tuned from the UV to the NIR range to coincide with any desired portion of the solar spectrum. The spectral characteristics of the absorption coefficient of NPs, such as the resonance peak strength and its position and broadening with respect to the solar radiation spectrum, determine the figure of merit (FoM) that quantifies the efficiency of solar radiation absorption. Toward achieving efficient solar energy absorption, the core–shell structure of NPs enables more flexible control of the optical properties of plasmon resonance by adjusting the shell thickness and/or core size as well as their material types.[22–25] For effective hot electron production and injection into the adjacent active semiconductor material, a nanoshell with a thin plasmonic shell can offer a larger optical field concentration in the shell region. In contrast, large-sized plasmonic NPs can generate a plasmon field spreading over a wider region in which the created hot electrons cannot survive to reach to the attached semiconductor during their lifetime, and unfavorably increase the fluctuations in carrier mobility. Additionally, the use of nanoshells lessens the plasmon radiative damping, which is significant for large-sized plasmonic materials, giving a greater chance for hot electron generation and utilization.[26,27] Numerous previous studies investigated plasmon-induced hot carriers in nanoshells for developing solar-energy harvesting devices.[22,28–30] Utilizing TiN as a shell in nanoshell structures for enhanced solar energy harvesting and photocatalytic applications is scarcely reported. Nevertheless, a previous study[31] suggests using hollow TiN nanoshells to accomplish efficient solar harvesting. In any of the prior works, no investigation into optimizing the geometrical parameters of nanoshells to achieve efficient solar energy absorption has been reported. Furthermore, the effects of radiative damping and optical field properties on the functionality of optimized nanoshells are disregarded.

In this paper, the Mie theory is applied to calculate the LSPR absorption spectra and the LSPR field of eccentric spherical TiN nanoshells, assuming two surrounding media (*i.e.*, air and water). For TiN nanoshells, we consider three core materials with different refractive indices and thermal conductivities (*i.e.*, air, silica (SiO_2), and magnesium oxide (MgO)). To quantify the solar absorption efficiency of the proposed nanoshells (hollow TiN, SiO_2–TiN and MgO–TiN nanoshells), we compute a FoM of an integrated absorption cross-section over the major spectral range of sunlight. It is shown that the LSPR of TiN nanoshells can be tuned sensitively over the entire UV-visible-IR region by varying the shell thickness and/or core size. Then, the solar absorption FoM can be adjusted by varying the geometrical parameters of the proposed TiN nanoshells. We compare the absorption FoM of the proposed TiN nanoshells and that of other NP composites including TiN, Au, and Ag nanospheres. It is demonstrated that, at optimal geometrical parameters, all structures (nanoshells and nanospheres) exhibit the maximum absorption FoM. The calculation of the LSPR electric field of TiN nanoshells demonstrates that the plasmon field is higher and more concentrated in the TiN shell which has a smaller volume than the TiN volume in TiN nanospheres. When comparing TiN nanoshells for their ability to absorb solar energy and their optical field properties, hollow TiN nanoshells outperform SiO_2–TiN and MgO–TiN nanoshells. It follows that hollow TiN nanoshells are more efficient than TiN nanospheres and other nanoshells in minimizing the unwanted scattering losses caused by the variation in the local charge carrier concentration and the radiative damping effects of LSPRs linked to the use of a large volume of plasmonic materials.

2. Methods and materials

Fig. 1 shows a schematic representation of a spherical TiN nanoshell which consists of a lossless dielectric core surrounded by a TiN shell and is embedded in a non-absorbing medium. Three different core materials (air, SiO_2, and MgO) are employed to examine the impact of the core material on the optical response of TiN nanoshells. The assumed core materials are nonabsorbing dielectrics with a relatively small permittivity and large band gap energy. Consequently, it is possible to negate the absorption of solar energy in the core as heat dissipation, and the hot electrons generated in the plasmonic TiN shell efficiently migrate into the attached semiconductor rather than the core region. Furthermore, in order to regulate the increase in the surface temperature of nanoshells, if required, the core materials are selected so as to have different thermal conductivities (κ). Our proposed core materials cover a wide range of thermal conductivities (κ) ranging from relatively low ($\kappa_{\text{air}} \approx 0.026$ W m^{-1} K^{-1})[32] through moderate ($\kappa_{\text{SiO}_2} \approx 1.38$ W m^{-1} K^{-1})[33] to high ($\kappa_{\text{MgO}} = 50$ W m^{-1} K^{-1}).[34] In Fig. 1, the radius of the core is R_c, the thickness of the TiN shell is d, and the total radius of the nanoshell is $R_s = R_c + d$. The dielectric functions of the core, shell, and host medium are denoted by ϵ_c, ϵ_s, and ϵ_m, respectively. In Fig. 1, the incident plane wave propagates in the positive z-direction where its electric vector $\boldsymbol{E}_0$ is linearly polarized in the x-direction. In the spherical coordinate system whose origin is at the center of the particle, the unit vectors are in the directions of r, θ, and ϕ. The plasmon fields parallel and perpendicular to the polarization direction of the incident field are computed by assuming $\theta = \pi/2$ and $\theta = 0$, respectively. In this work, we consider two host media for NP structures, air and water, representing common media in plasmon-enhanced solar energy conversion systems, such as thin-film solar cells for which the plasmonic NPs deposited at their top surface,[35] aqueous-based solar cells,[36] and photocatalytic water splitting.[37] The synthesis feasibility of the semiconductor core–TiN shell containing TiN hollow spheres has been reported in various previous studies.[38–40]

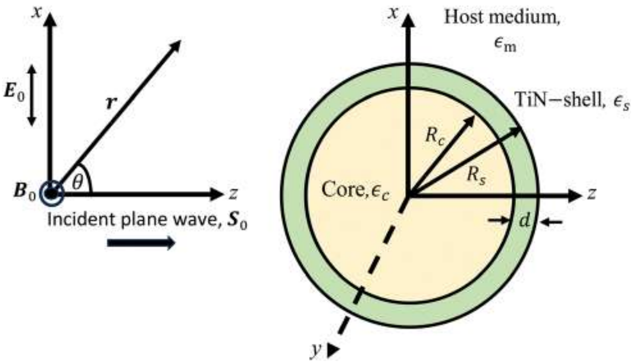

Fig. 1 A plane wave incident upon a concentric spherical TiN nanoshell: R_c is the core radius, d is the shell thickness, and R_s is the total particle radius. ϵ_c, ϵ_s, and ϵ_m denote the dielectric functions of the core, shell, and embedding medium, respectively. A plane wave with an intensity $\boldsymbol{S}_0$ propagates in the positive z-direction, while $\boldsymbol{E}_0$ is the incident electric field vector polarized in the x-direction.

The primary indicator of the optical response of plasmonic NPs is the non-dimensional absorption (scattering) efficiency $Q_{\text{abs}}(Q_{\text{sca}})$ that represents the ratio of the absorbed (scattered) power $P_{\text{abs}}(P_{\text{sca}})$ to the incident power P_0. In this study, we employ the Mie theory-based approach of Aden and Kerker[41,42] to investigate the optical response of spherical nanoshells. In a previous study,[41] the authors developed an analytical solution to Maxwell's equations that describe the scattering and absorption of light by spherical nanoshells. The theoretical approach[41] is based on the Mie theory[43] of light scattering by concentric isotropic spheres. The radiation field in the core, shell, and medium regions are calculated using Mie-like coefficients that are denoted by a_n and b_n, where the scattering and extinction coefficients are given by:[41,42]

$$Q_{\text{sca}} = \left(\frac{2}{\alpha^2}\right)\sum_{n=1}^{\infty}(2n+1)\left[\text{Re}\left(|a_n|^2 + |b_n|^2\right)\right], \tag{1}$$

$$Q_{\text{ext}} = \left(\frac{2}{\alpha^2}\right)\sum_{n=1}^{\infty}(2n+1)[\text{Re}(a_n + b_n)], \tag{2}$$

where $\alpha = 2\pi(R_s/\lambda)$ is a size parameter and λ is the wavelength of light. Using eqn (1) and (2), one can obtain the absorption coefficient $Q_{\text{abs}} = Q_{\text{ext}} - Q_{\text{sca}}$. The expressions of electric field in each region of nanoshells are given in terms of the coefficients a_n and b_n.[41] Using the algorithms of Toon and Ackerman,[44] we developed a code in MATHCAD software to calculate the absorption coefficient of spherical nanoshells and the electric field in each of their respective regions (core, shell, and medium). The formulations of the parameters a_n and b_n shown in eqn (1) and (2), which include the Riccati–Bessel functions and their derivatives, have been reformed.[44] Our code demonstrates that the algorithms of Toon and Ackerman are numerically accurate and stable for all refractive indices, large and small particles, and cores of any relative size.

In order to estimate the viability of NP structures for solar energy conversion, we define an integrated absorption cross-section FoM, $\mathrm{IQ_{abs}}$, in the form of[45]

$$\mathrm{IQ_{abs}} = \int_{300\mathrm{nm}}^{2000\mathrm{nm}} Q_{\mathrm{abs}}(\lambda)E(\lambda)\mathrm{d}\lambda, \tag{3}$$

where $E(\lambda)$ is the sun's spectral irradiance in W m^{-2} nm^{-1}. It is worth noting that the FoM of solar energy absorption $\mathrm{IQ_{abs}}$ provides a reliable indication regarding solar energy harvesting with little information about the extraction and transport efficiency of the generated free charge carriers (*e.g.*, hot electrons), where the other factors play a significant role in that process. As the volume of the plasmonic material increases, various adverse effects that limit the effectiveness of the generated hot electrons are increased and thus the number of electrons reaching the attached semiconductor surface could be significantly decreased. These drawbacks are attributed to three main factors: the first is the heat caused by the non-radiative relaxation of surface plasmon modes. This generated heat can distort the shape, local field, and optical response of the NPs, thus affecting the generated hot electron density and dynamics. The second is the increase in the electron–electron scattering losses linked to localized variations in the mobility of the charge carriers. The spatial variation of the carrier mobility is due to the fluctuation in the concentration of hot electrons produced by surface plasmon decay at various positions within the NPs. The third is the radiative damping effects associated with spontaneously emitted photons by the oscillating electrons. Since hot electron generation is mainly related to nonradiative LSPR decay, a decrease in hot electron generation and utilization is anticipated for systems with large radiative damping rates. The radiative damping rate is proportional to the number of free electrons in the particle and then to the particle's size. For instance, the radiative damping begins to suppress the LSPR of Au and Ag nanospheres when the nanosphere radius approximately exceeds 15 nm and 25 nm, respectively.[46] The interplay between all of the aforementioned factors can be advantageously mitigated by employing the nanoshell structure, in which the plasmon mode field is concentrated in the thin shell region and the highest electron generation occurs near the shell surface. Furthermore, compared to a solid nanosphere, the maximum solar absorption in the nanoshell structure can be achieved at a lower plasmonic material volume. Consequently, the radiative damping deterioration becomes less significant giving a higher chance for hot electron utilization.

The absorbed light eventually dissipated as heat due to the nonradiative relaxation of the LSPR which is characterized by the electron–phonon scattering time $\tau_{\mathrm{e-ph}}$ ($\tau_{\mathrm{e-ph}} \approx 19.5$ ps and 3 ps for TiN and Au, respectively).[47] The electron–phonon relaxation time is independent of particle size and shape.[48] When the light absorption is significantly enhanced, the elevated temperature of NPs possibly heats the materials surrounding them, hastening the deterioration of the device functionality. Therefore, in this study, we will examine the effect of temperature increase on the production, transportation, and hence utilization of hot electrons in the nanostructure.

As the steady-state temperature distribution $T(r)$ inside and outside the NPs (or nanoshell) is reached under continuous-wave illumination, the temperature increase of NPs with different shapes is given by[49]

$$\Delta T = \frac{\sigma_{\mathrm{abs}} I}{4\pi\kappa_{\mathrm{med}}\beta R_{\mathrm{eq}}}, \tag{4}$$

In eqn (4), $\sigma_{\mathrm{abs}} = Q_{\mathrm{abs}}A_{\mathrm{p}}$ is the absorption cross-section where $A_{\mathrm{p}} = \pi R_{\mathrm{s}}^2$ is the particle cross-sectional area projected onto a plane perpendicular to the incident light and I is the irradiance of the illuminating light (power per unit surface).[50] β is a dimensionless geometrical correction factor where $\beta = 1$ for spherical NPs (*i.e.*, nanoshells or homogeneous spherical NPs). R_{eq} is the radius of a solid spherical particle having an equivalent volume of the plasmonic region in the NP structure under consideration. For nanoshells, considering that the heating is primarily delivered from the shell region to the core and surrounding medium, it can be assumed that $R_{\mathrm{eq}} = (R_{\mathrm{s}}^3 - R_{\mathrm{c}}^3)^{1/3}$. For homogeneous spherical NPs, $R_{\mathrm{eq}} = R_{\mathrm{c}}$. In the case of nanoshells, the core region is considered as another contact medium for heat diffusion, in addition to the host medium of nanoshells. κ_{med} is the thermal conductivity of the surrounding medium of the NPs. When the plasmonic region (TiN shell in the nanoshell structure) is located close to the interface of two media with different thermal conductivities, κ_{med} is considered as the average thermal conductivity of the two media.[51] For nanoshells, κ_{med} shown in eqn (4) is the average thermal conductivity of the core and embedding media, while in the homogenous spherical particles κ_{med} is the conductivity of the embedding medium.[51]

Involving the correction of the electron scattering at a material surface, the dielectric function of the core (or shell) can be calculated using the Lorentz–Drude theory by[52]

$$\epsilon(r_{\mathrm{eff}},\omega) = \epsilon(\omega)_{\mathrm{exp}} + \frac{{\omega_{\mathrm{p}}}^2}{\omega^2 + j\omega\Gamma_0} - \frac{{\omega_{\mathrm{p}}}^2}{\omega^2 + j\omega\Gamma_{\mathrm{mod}}}, \tag{5}$$

where $\epsilon(\omega)_{\mathrm{exp}}$ is the experimental bulk dielectric function, ω_{p} is the plasma frequency, and Γ_{mod} is the corrected bulk collisional frequency that includes size-dependent electron scatterings, given by

$$\Gamma_{\mathrm{mod}} = \Gamma_0 + A\frac{v_{\mathrm{f}}}{r_{\mathrm{eff}}}, \tag{6}$$

where Γ_0 is the bulk collisional frequency, r_{eff} is the mean free path of free electrons (*i.e.*, $r_{\mathrm{eff}} = 2R_{\mathrm{c}}$ for spherical plasmonic NPs and $r_{\mathrm{eff}} = d$ for spherical nanoshells with a plasmonic shell of thickness d), v_{f} is the Fermi velocity, and A is a theory-dependent parameter and depends on the characteristics of the scattering process (*e.g.* isotropic or diffuse scattering) as well. In this study, the parameter A is assumed to have a value of 1.[52] In eqn (5), the experimental bulk complex dielectric function of TiN is obtained from the experimental data reported by Edlou *et al.*,[53] and those of Au and Ag are obtained from the experimental data of Johnson and Christy.[54] It is worth pointing out that the experimental data of the real and imaginary parts of TiN permittivity published in a previous study[53] exhibit approximately the average of various experimental data reported by several groups worldwide.[55] For the electron concentration n_e of TiN in the range of $(1.6–6.6) \times 10^{22}$ cm^{-3}, the effective mass of an electron m_e^* is correspondingly in the range of $(1.7–3.1)m_e$.[56] By considering this range of m_e^* and n_e for estimating the Fermi velocity $v_f = (\hbar/m_e^*)(3\pi^2 n_e)^{1/3}$, one finds that the damping rate due to the surface scattering (Av_f/r_{eff}) becomes comparable to the bulk electron scattering $\Gamma_0 \approx 0.2–0.6$ eV[57] when $r_{eff} < 1$ nm which is smaller than the assumed TiN shell (or core) sizes in this study. Therefore, the damping rate of electron–surface collisions for TiN, which is represented by the second term on the right-hand side of eqn (6), can be neglected (*i.e.*, $\epsilon(r_{eff}, \omega) \approx \epsilon(\omega)_{exp}$ in eqn (5) for TiN). In contrast, the surface damping plays a major role in the case of Au and Ag plasmonic particles where $\Gamma_0 \approx 0.053$ eV and 0.048 eV,[58] and $v_f \approx 1.4 \times 10^8$ cm s^{-1} and 1.39×10^8 cm s^{-1} for Au and Ag,[59] respectively. In our calculations, the values of the plasma frequency are assumed to be as reported in a previous study,[58] where $\hbar\omega_p \approx 9.03$ eV and 9.01 eV for Au and Ag, respectively.

In this study, the dielectric functions of core materials are computed using the expressions:

$$\epsilon_c = 1 + \frac{0.6961663\lambda^2}{\lambda^2 - (0.0684043)^2} + \frac{0.4079426\lambda^2}{\lambda^2 - (0.1162414)^2} + \frac{0.8974794\lambda^2}{\lambda^2 - (9.896161)^2}, \tag{7}$$

$$\epsilon_c = 2.956362 - 0.01062387\lambda^2 - 0.0000204968\lambda^4 + \frac{0.02195770}{\lambda^2 - 0.01428322}, \tag{8}$$

for SiO_2[60] and MgO,[61] respectively. λ in eqn (7) and (8) is in μm.

3. Results and discussion

3.1. Geometrical optimization

First, we spot on the geometrical optimization of the TiN nanoshell for achieving maximum solar absorption. The commonly reported dielectric SiO_2 core is initially used as a core material for exploring the common absorption characteristics of the optimized TiN nanoshells. Next, other selected core materials, air and MgO, are employed to explore the influence of the core material on the plasmonic and thermal properties of the TiN nanoshell. Based on the observed results and taking into account the temporal dynamics of photoexcited electrons in TiN, we present detailed discussions on the superiority of employing TiN nanoshells over TiN homogenous spheres in hot-carrier devices.

For SiO_2–TiN core–shell NPs, Fig. 2a and b illustrates the variation of the FoM for solar energy absorption (IQ_{abs}) with the normalized shell thickness with respect to the core radius d/R_c at different values of R_c and in the limit of $d \leq R_c$. In Fig. 2a and b, IQ_{abs} is calculated when the surrounding medium is air $(n_m = \sqrt{\epsilon_m} = 1.0)$ and water (n_m = 1.333), respectively. It is shown that when $R_c \geq 40$ nm, IQ_{abs} exhibits a peak at a specific d/R_c ratio based on the embedding medium. When $R_c < 40$ nm, the peak of IQ_{abs} does not appear in the assumed range of the shell thickness ($d \leq R_c$). The latter behavior will be explained in detail in Fig. 3 and 4. It is evident from Fig. 2a and b that IQ_{abs} reaches its highest maximum magnitude when R_c = 80 nm and d = 16 nm (d/R_c = 0.2) and when R_c = 50 nm and d = 20 nm (d/R_c = 0.4) in air and water media, respectively. The increase in the refractive index of the surrounding medium leads to a red shift of the LSPR band and an enhancement in the absorption efficiency associated with a reduction in the scattering efficiency.[62] Therefore, the magnitude of the absorption coefficient $Q_{abs}(\lambda)$ obtained in water, and consequently IQ_{abs}, is larger than that obtained in air. Fig. 2c and d shows the variation of the IQ_{abs} of TiN, Au, and Ag nanospheres with a radius of R_c when immersed in air and in water, respectively. It is shown that TiN nanospheres exhibit a higher maximum of IQ_{abs} compared to those of Au and Ag nanospheres in air and water media. In the case of TiN nanospheres, the maximum of IQ_{abs} occurs when R_c = 80 nm and R_c = 60 nm in air and water, respectively. From Fig. 2c and d, one finds that the maximum of IQ_{abs} of TiN nanospheres is greater than that of Au nanospheres by a factor of ∼1.48 and ∼1.33 in air and water, respectively. When R_c = 80 nm and R_c = 50 nm, SiO_2–TiN nanoshells reveal the highest maximum of IQ_{abs} which is about ∼1.25 and ∼1.12 greater than the maximum values of IQ_{abs} for TiN nanospheres in air and water, respectively. Interestingly, in Fig. 2a and b, it is shown that the highest maximum of IQ_{abs} occurs at thinner shell thicknesses in comparison to those at which the maximum of IQ_{abs} is found. For instance, in Fig. 2a, when the medium is air, IQ_{abs} reaches its highest maximum (∼1386) at d = 16 nm when R_c = 80 nm, while its other maximums at other different values of R_c ($R_c \neq 80$ nm) occur at larger values of d. For the water medium, Fig. 2b shows a similar trend. In water, IQ_{abs} reaches its highest maximum (∼2761) at d = 20 nm when R_c = 50 nm.

The absorption FoM IQ_{abs} is obtained by the convolution integral in eqn (3) which represents the overlap amount of the absorption coefficient Q_{abs} and the spectral irradiance of the sun E. Therefore, the spectral distribution matching between Q_{abs} and E, in addition to the large magnitude of Q_{abs}, is a crucial factor to achieve a high IQ_{abs} and hence high solar energy harvesting. For SiO_2–TiN nanoshells, Fig. 3a and b shows the spectra of the absorption coefficient Q_{abs} calculated using the Mie theory when R_c = 80 nm and R_c = 50 nm in air and water media, respectively, at different shell thicknesses. At these core radiuses, the highest maximum of IQ_{abs} for SiO_2–TiN nanoshells is achieved in air and water, respectively. From Fig. 3a and b, it is observed that the LSPR peak blueshifts as the shell thickness d increases, permitting a controllable spectral overlap between Q_{abs} and E. The blueshift of the LSPR peak in Fig. 3a and b reflects the dominant role of increasing TiN material amount whose LSPR peak tends to locate in the visible range at approximately 600 nm. In Fig. 3a and b, there are two peaks in the absorption spectra of thick TiN shells of d = 32 nm and 25 nm in air and water (red-colored lines), respectively; the first peak is associated with the dipolar LSPR mode at $\lambda \approx$ 600 nm, while the second peak corresponds to the quadrupole mode at $\lambda \approx 800$ nm. With increasing the TiN shell thickness d, Q_{abs} is increased in magnitude and reaches the maximum at

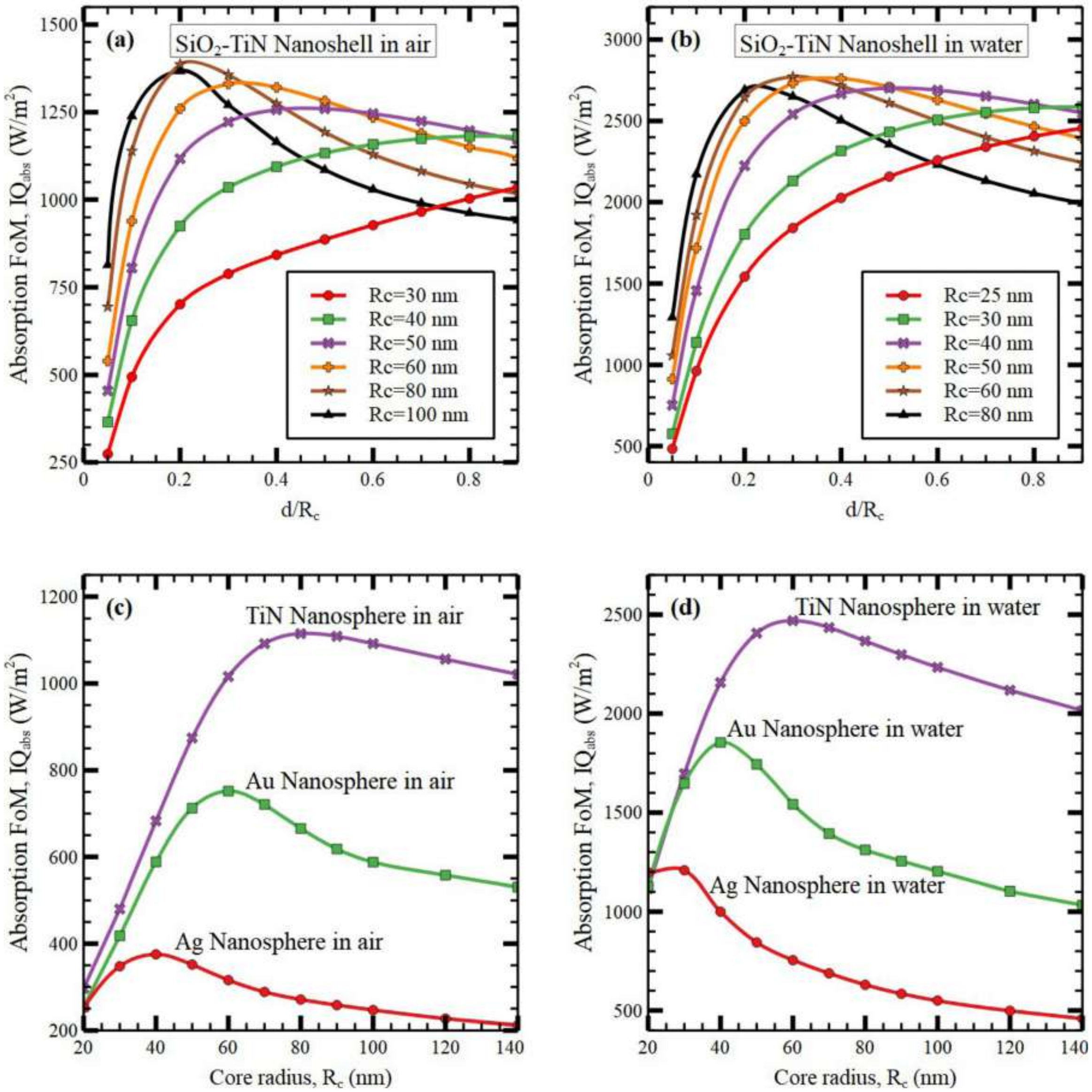

Fig. 2 For SiO_2–TiN nanoshells, the FoM of solar energy absorption IQ_{abs} *versus* the normalized shell thickness with respect to the core radius d/R_c at different values of R_c when the embedding medium is (a) air and (b) water. For TiN, Au, and Ag nanospheres, IQ_{abs} *versus* the core radius R_c in (c) air and (d) water.

d = 16 nm and 15 nm in the case of air and water media (green-colored lines), respectively. As the TiN shell thickness d increases further, the scattering efficiency surpasses the absorption efficiency. Concurrently, as the thickness of the shell increases, the plasmon resonance peak broadens due to multipolar LSPR modes. As shown in Fig. 3a and b, IQ_{abs} reaches its maximum when d = 16 nm and 20 nm in air and water, respectively. As previously indicated, the maximum of Q_{abs} does not always imply the maximum of IQ_{abs} for the given NP structure parameters where the good overlapping between the spectral distribution of Q_{abs} and that of the sun's spectral irradiance E plays an important role in determining IQ_{abs}. For instance, in the case of SiO_2–TiN nanoshells embedded in water, the maximum of Q_{abs} and IQ_{abs} occurs at different values of the shell thickness. In Fig. 3c and d devoted to TiN nanospheres, the maximum of IQ_{abs} occurs at R_c = 80 nm and 60 nm. At these R_c values, the spectral distributions of Q_{abs} and E are well matched, and in spite of Q_{abs} not being the maximum, the convolution integral of IQ_{abs} is the maximum. From Fig. 3a–d, it can also be observed that the full width at half-maximum (FWHM) of the absorption spectrum of SiO_2–TiN nanoshells is wider than that of TiN nanospheres, approximately by a factor of 1.35 and 1.25 when the highest maximum of IQ_{abs} is achieved in air and water, respectively. Therefore, the convolution of Q_{abs} and E in eqn (3) becomes more efficient, and consequently IQ_{abs} becomes higher, in the cases of nanoshells compared to the cases of nanospheres as shown in Fig. 2.

3.2. Effects of the core material

The type of dielectric core material plays a crucial role in the performance and characteristics of core–shell plasmonic systems.[63,64] The choice of the dielectric core can significantly

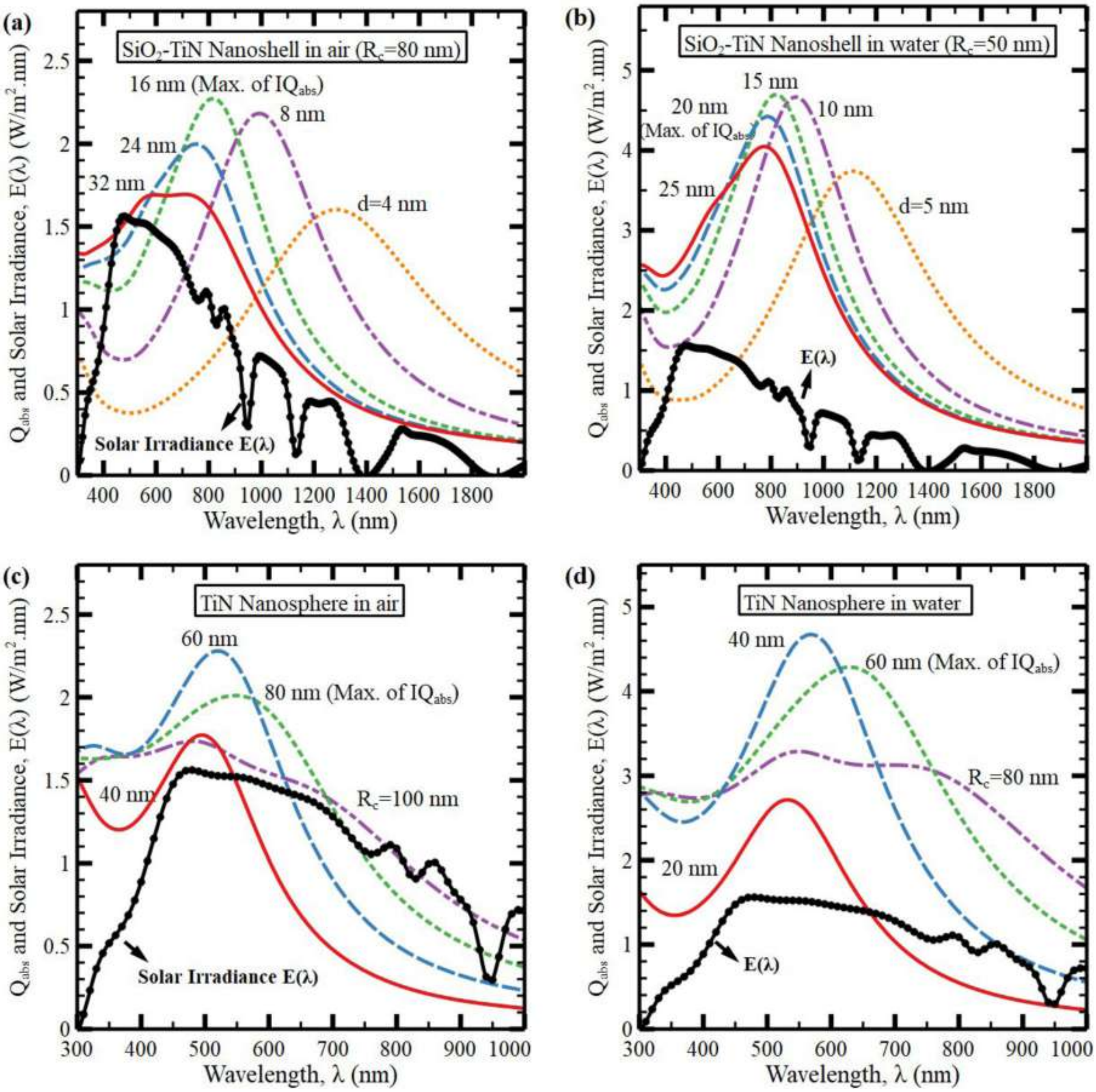

Fig. 3 The spectra of the absorption coefficient Q_{abs} for SiO_2–TiN nanoshells at different values of the shell thickness d in air (a) and water (b) and for TiN nanospheres at different values of the particle radius R_c in air (c) and water (d). For SiO_2–TiN nanoshells, we choose the core radius R_c = 80 nm and 50 nm for air and water media, respectively, at which IQ_{abs} shows the highest maximum at a specific value of d. The solar irradiance on the earth is also shown in these figures. Using different maxima, the scale of the vertical axis for air and for water makes the solar spectrum look different particularly for (c) and (d); also the x-axis scale is deceiving between (a) and (b) on one hand and between (c) and (d) on the other. In unifying the horizontal and vertical axis ranges, it will show well how the optical characteristics of the TiN nanoshell are tuned and broadened over the solar spectrum relative to the nanosphere system and how the external medium significantly affects the absorption intensity of LSPR systems.

influence the optical, plasmonic, and energy-related properties. The polarizability of the core material can alter the local electric field distribution around the plasmonic shell, affecting the plasmonic resonance frequency, intensity and broadening. Now, let us attempt to attain greater solar energy absorption at optimum geometrical parameters of TiN nanoshells by utilizing various core dielectric materials. In Fig. 4a and b, we plot IQ_{abs} for hollow TiN (air core) and MgO–TiN nanoshells embedded in water *versus* d/R_c at different core radii, R_c, respectively. To reduce the number of figures in this paper, we do not show the variation between IQ_{abs} and d/R_c for hollow TiN and MgO–TiN nanoshells embedded in air; however, the key findings will be provided in Table 1a and b. In the cases of air and water media, it is observed that the hollow TiN nanoshells exhibit larger maximums of IQ_{abs} in comparison to SiO_2–TiN and MgO–TiN nanoshells. For SiO_2–TiN and MgO–TiN nanoshells in the water medium, the highest maximum of IQ_{abs} is attained when R_c = 50 nm and d = 20 nm (d/R_c = 0.4), while for hollow TiN nanoshells the highest maximum of IQ_{abs} is attained when R_c = 50 nm and d = 15 nm (d/R_c = 0.3). The highest maxima of IQ_{abs} are 2861 W m^{-2}, 2761 W m^{-2}, and 2711 W m^{-2} for hollow TiN, SiO_2–TiN, and MgO–TiN nanoshells, respectively. The highest maxima of IQ_{abs} of these nanoshells are higher than the maximum of IQ_{abs} of TiN

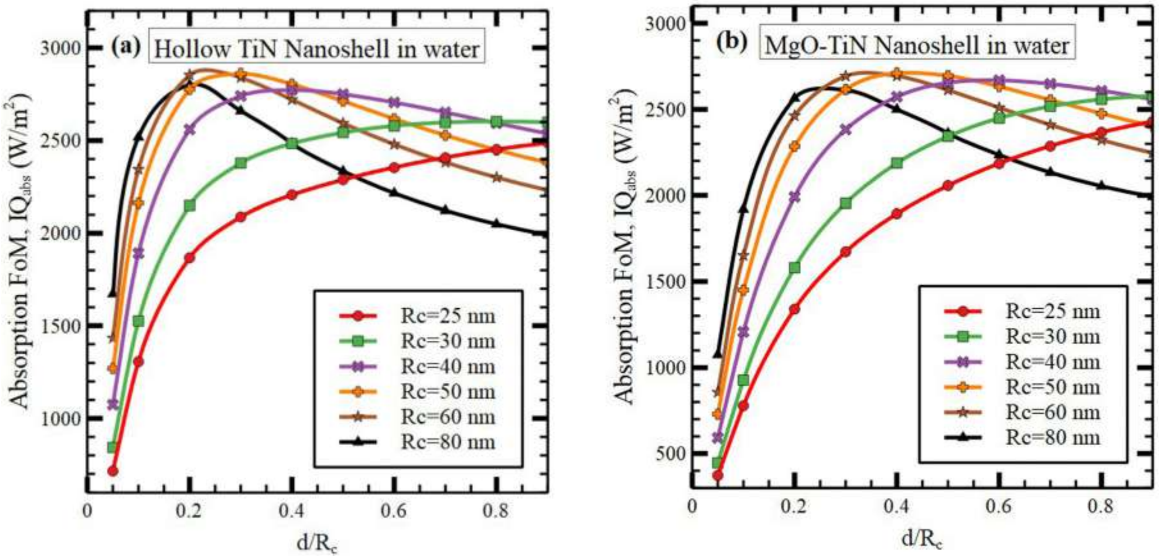

Fig. 4 The FoM of solar energy absorption IQ_{abs} against d/R_c at different values of R_c for (a) hollow TiN nanoshells and (b) MgO–TiN nanoshells embedded in water.

homogeneous nanospheres embedded in water by factors of ∼1.16, 1.12, and 1.1, respectively. For the air medium, it is found that the highest maximum of IQ_{abs} for hollow TiN, SiO_2–TiN, and MgO–TiN nanoshells occurs at the same geometrical parameters, namely $R_c = 80$ nm and $d = 16$ nm ($d/R_c = 0.2$). The highest maxima of IQ_{abs} are 1513 W m^{-2}, 1386 W m^{-2}, and 1336 W m^{-2} for hollow TiN, SiO_2–TiN, and MgO–TiN nanoshells, respectively. The highest maxima of IQ_{abs} of the nanoshells are ∼1.35, 1.24, and 1.2 times the maximum of IQ_{abs} of TiN homogeneous nanospheres embedded in air, respectively.

In core–shell nanostructures, the hybridization theory[65] suggests that the surface plasmons are generated at the inner (cavity mode) and on the outer plasmonic shell (sphere mode). The sphere and cavity plasmons hybridize to form a red-shifted coupled (symmetric or dipole-like) plasmon mode and a blue-shifted anti-coupled (asymmetric) mode. It is worth noting that the asymmetric mode is not apparent in the computed spectra in Fig. 3, which shows only the symmetric plasmon mode (lower frequency sphere plasmon mode). The strength of plasmon coupling depends on the plasmonic shell thickness and the dielectric constant of the core material. As the shell thickness and/or the core dielectric constant decrease, the strength of the coupling and the energy difference between the two resulting plasmon modes increase.[64] Furthermore, the LSPR peaks of nanoshells are broadened and the intensity of the LSPR peaks is slightly decreased with decreasing the shell thickness and/or the core dielectric constant.[64] The latter behavior can be observed in Fig. 3a and b. Based on this, as the core dielectric constant decreases, the profile of the absorption spectra of TiN nanoshells can be efficiently well-matched with the irradiance spectra of the sun over a wider spectrum range. Therefore, the absorption FoM of hollow TiN with the

Table 1 (a) For hollow TiN, SiO_2–TiN, and MgO–TiN nanoshells, the optimized geometrical parameters of nanoshells and the corresponding highest maximum of $IQ_{abs}(IQ_{abs}^{H\text{-}max})$ in both air and water media. The core radius R_c and the shell thickness d are in nm and $IQ_{abs}^{H\text{-}max}$ is in W m^{-2}. (b) For TiN, Au, and Ag homogeneous nanospheres, the optimized geometrical parameters of nanospheres and the corresponding maximum of $IQ_{abs}(IQ_{abs}^{Max})$ in both air and water media. The core radius R_c and the shell thickness d are in nm and IQ_{abs}^{Max} is in W m^{-2}

(a)

Hollow TiN nanoshells						SiO_2–TiN nanoshells						MgO–TiN nanoshells					
In air			In water			In air			In water			In air			In water		
R_c	d	$IQ_{abs}^{H\text{-}max}$	R_c	d	$IQ_{abs}^{H\text{-}max}$	R_c	d	$IQ_{abs}^{H\text{-}max}$	R_c	d	$IQ_{abs}^{H\text{-}max}$	R_c	d	$IQ_{abs}^{H\text{-}max}$	R_c	d	$IQ_{abs}^{H\text{-}max}$
80	16	1513	50	15	2861	80	16	1386	50	20	2761	80	16	1336	50	20	2711

(b)

TiN nanospheres				Au nanospheres				Ag nanospheres			
In air		In water		In air		In water		In air		In water	
R_c	IQ_{abs}^{Max}	R_c	IQ_{abs}^{Max}	R_c	IQ_{abs}^{Max}	R_c	IQ_{abs}^{Max}	R_c	IQ_{abs}^{Max}	R_c	IQ_{abs}^{Max}
80	1115	60	2470	60	751.95	50	1744	40	375.34	30	1208

lowest core dielectric constant is higher than that of other nanoshells, as shown in Fig. 2b and 4a, b.

In Table 1a and b, we list the optimized geometrical parameters of the proposed nanoshells and homogenous nanospheres at which the highest maximum of $\mathrm{IQ_{abs}}(\mathrm{IQ_{abs}^{H\text{-}max}})$ and the maximum of $\mathrm{IQ_{abs}}(\mathrm{IQ_{abs}^{Max}})$ are achieved, respectively, in both air and water media. Let us close this section by pointing out the fundamental observation that the hollow TiN nanoshells with the lowest core refractive index, and consequently the highest light trapping capability in the core, exhibit the highest FoM of solar energy absorption than the other nanoshells (SiO_2–TiN and MgO–TiN nanoshells) and TiN nanospheres.

3.3. Optimized TiN nanoshells for enhancing hot electron generation

Above, in order to achieve greater solar energy absorption, we focused on optimizing the geometrical parameters of TiN nanoshells embedded in air and water assuming various core dielectric materials (air, SiO_2, and MgO). It is found that hollow TiN nanoshells with the lowest core permittivity of air exhibit the highest solar absorption in comparison to SiO_2–TiN and MgO–TiN nanoshells. While the highly solar energy absorption is undoubtedly an important factor, other optical and thermal phenomena also play a fundamental role in determining the effectiveness of utilizing these TiN nanoshells in hot-electron-related applications. These factors are related to the decaying mechanisms of the LSPR and the temporal dynamics of generated hot electrons within the plasmonic nanoshells depicted in Fig. 5a and b. As shown in Fig. 5a, LSPR is decayed through two main mechanisms, the radiative damping in the form of spontaneous emission and nonradiative damping, generating hot electrons. The hot electrons can be injected into the conduction band of the attached semiconductor in photoelectric conversion devices, where they gain a much longer lifetime

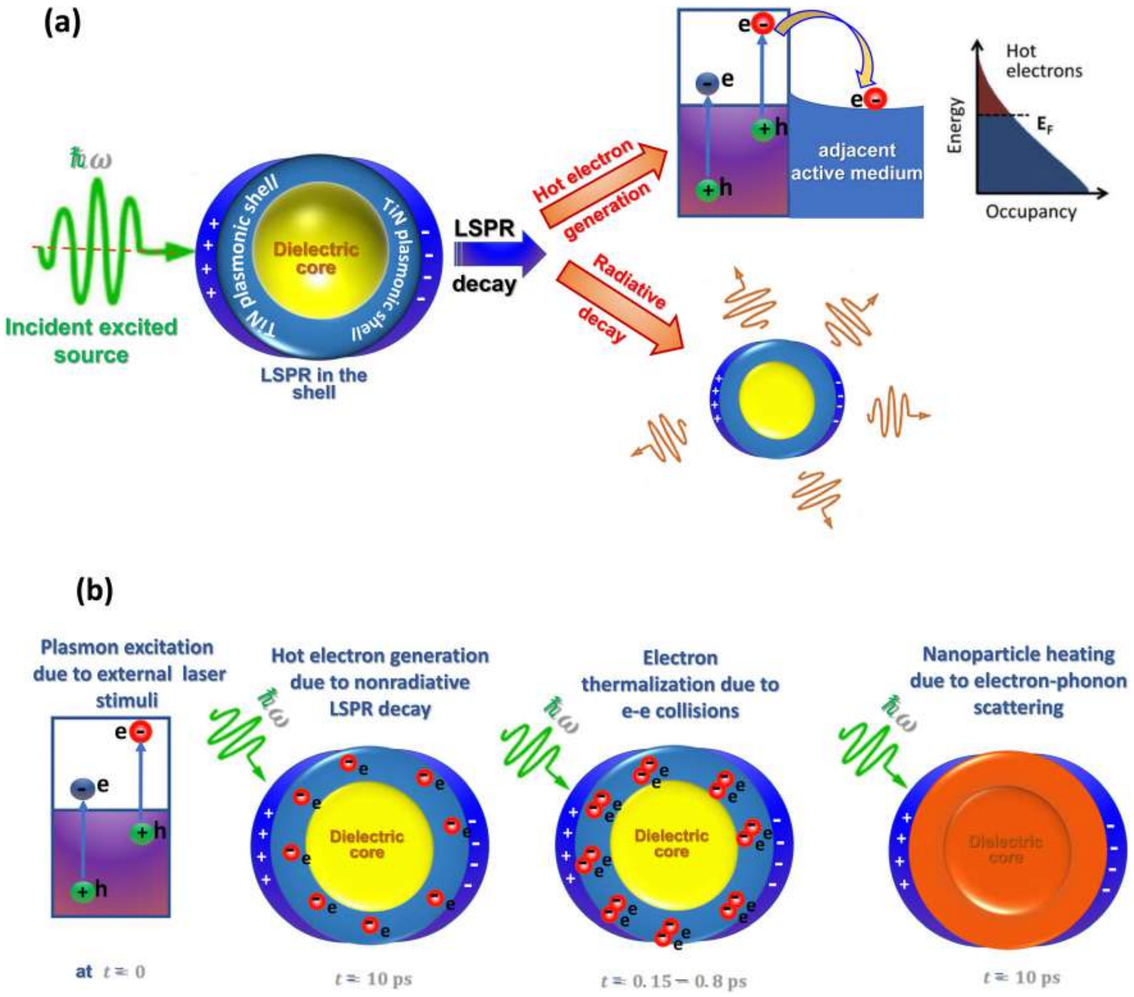

Fig. 5 Illustration of the decay processes of LSPR and the temporal dynamics of generated hot electrons in the dielectric–TiN core–shell system. (a) The photoinduced LSPR in the TiN conductive shell is decayed through two possible mechanisms: (i) energy-wasted radiative damping, in which photons are spontaneously emitted from the coherently oscillating electrons, or (ii) hot electron generation in which an electron near the Fermi energy (E_F) absorbs LSPR photons and gets excited far above E_F. Theses hot electrons can be utilized in activating an adjacent active medium for enhanced catalytic and photovoltaic applications. (b) Dynamical processes of the short-lived hot electrons in the dielectric–TiN core–shell system, *i.e.*, from formation to nanoparticle heating.

Table 2 (a) τ_{rad} and IQ_{abs} of hollow TiN nanoshells and TiN nanospheres in air medium. For hollow TiN nanoshells, we assume R_c = 60 nm, 70 nm, and 80 nm and the shell thickness d is variable. For TiN nanospheres, we assume R_c = 20–80 nm. (b) τ_{rad} and IQ_{abs} of hollow TiN nanoshells and TiN nanospheres in water medium. For hollow TiN nanoshells, we assume R_c = 30 nm, 40 nm, and 50 nm and the shell thickness d is variable. For TiN nanospheres, we assume R_c = 35–65 nm

(a)

Hollow TiN nanoshells in air									
	R_c = 60 nm		R_c = 70 nm		R_c = 80 nm		TiN nanospheres in air		
d/R_c	τ_{rad} (fs)	IQ_{abs} (W m^{-2})	τ_{rad} (fs)	IQ_{abs} (W m^{-2})	τ_{rad} (fs)	IQ_{abs} (W m^{-2})	R_c (nm)	τ_{rad} (fs)	IQ_{abs} (W m^{-2})
0.6	0.65	1236	0.56	1183	0.42	1129	20	32.77	296.5
0.5	0.88	1292	0.70	1249	0.51	1194	30	10.12	480.01
0.4	1.28	1355	0.88	1332	0.64	1283	40	4.45	682.84
0.3	1.98	1416	1.36	1426	0.99	1397	50	2.37	874
0.2	3.75	1445	2.56	1502	1.86	1513	60	4.81	1016
0.1	**12.0**	**1275**	**7.94**	**1381**	5.56	1452	70	1.00	1092
0.05	41.2	860	26.88	960	18.65	1044	80	1.59	1115

(b)

Hollow TiN nanoshells in water									
	R_c = 30 nm		R_c = 40 nm		R_c = 50 nm		TiN nanospheres in water		
d/R_c	τ_{rad} (fs)	IQ_{abs} (W m^{-2})	τ_{rad} (fs)	IQ_{abs} (W m^{-2})	τ_{rad} (fs)	IQ_{abs} (W m^{-2})	R_c (nm)	τ_{rad} (fs)	IQ_{abs} (W m^{-2})
0.6	4.98	2578	2.47	2706	1.49	2617	35	7.08	1951
0.5	6.69	2543	3.27	2751	1.97	2713	40	5	2157
0.4	9.67	2484	4.58	2773	2.68	2805	45	3.63	2309
0.3	16	2378	7.24	2741	4.22	2861	50	2.79	2407
0.2	31	2149	**14.22**	**2560**	**7.92**	**2777**	55	2.2	2457
0.1	108	1525	47.46	1892	25.77	2162	60	1.81	2470
0.05	400	842	172.8	1074	91.84	1270	65	1.49	2460

(up to milliseconds). As shown in Fig. 5b, the plasmonic hot electrons/holes are excited as a result of the nonradiative decay of surface plasmons. Then, the excess energy in the hot electrons, which are sometimes called nonthermal electrons, is subsequently distributed amongst the thermal electrons *via* electron–electron scattering processes. This process is characterized by a thermalization time, τ_{th}. The electron–phonon scattering mechanism characterized by an electron–phonon scattering time, τ_{e-ph}, leads to a lattice thermalization process in which the hot electrons lose their energy to the lattice resulting in an increase in the local nanoshell temperature. The energy of phonons is lost until the electron and lattice temperatures approach an equilibrium value, at a rate equal to the phonon–phonon scattering rate influenced by the temperature gradient and thermal conductivity of the NP material. To comprehend the viability of using the hot electrons produced in the TiN nanoshell structure for beneficial purposes, we will embark to investigate the restrictions on the nanoshell design for eliminating (or minimizing) the effect of energy loss channels on the dynamics of hot electrons. In addition, the optical field distribution of the LSPR will be computed in order to address how the nanoshell design affects the creation and propagation of hot electrons within the IQ_{abs} optimized TiN nanoshells.

In view of the previously described temporal dynamics of hot electrons, hot electrons require fast carrier extraction and utilization, at least within the thermalization time τ_{th}. Therefore, the relaxation time associated with energy loss channels in the TiN nanoshell should be smaller than or at least comparable to the thermalization time τ_{th} as much as possible. In the literature, inconsistent reports on the value of τ_{th} have been reported for TiN ranging from ~0.15 to 0.8 ps.[66–69] It has been reported that the thermalization time can be increased by introducing nitrogen vacancies that reduce the electron density in the band structure and exhibit smaller linewidths of optical phonon bands indicating weaker electron–phonon coupling.[69] In this paper, we accept the lowest value of τ_{th} = 0.15 ps[69] to guarantee the highest utilization of the generated hot electrons. The central damping mechanism of the surface plasmons is the radiative damping of the oscillating electrons by the spontaneous emission. The radiation damping time of the plasmon oscillations τ_{rad} is inversely proportional to the number of free electrons in the particle N_e, and consequently the volume of the plasmonic material, given by[70]

$$\tau_{rad} = \frac{12\pi\varepsilon_0 m_e^* c^3}{2e^2 {\omega_{sp}}^2 \sqrt{\varepsilon_m}} \frac{1}{N_e}. \tag{9}$$

In eqn (9), ω_{sp} is the resonance plasmon frequency and $N_e = n_e V_p$ where n_e is the electron density and V_p is the volume of the plasmonic material, so that $V_p = (4\pi/3)({R_s}^3 - {R_c}^3)$ for nanoshells and $V_p = (4\pi/3){R_c}^3$ for nanospheres. It is worth noting that the expression of τ_{rad}[70] is given using the CGS system, while we use the MKS system in eqn (9). In Table 2a and b, assuming n_e = 1.6×10^{22} cm^{-3} (@58% N) where $m_e^* = 1.7m_e$,[56] we report the radiative damping time τ_{rad} and IQ_{abs} for hollow TiN nanoshells and TiN nanospheres, respectively, in air and water. In Table 2a and b, we list the values of τ_{rad} and IQ_{abs} for hollow TiN nanoshells and TiN homogenous nanospheres in air and water, respectively. For hollow TiN nanoshells, we vary the shell thickness at each core radius R_c where R_c = 60 nm, 70 nm, and 80 nm in air and R_c = 30 nm, 40 nm, and 50 nm in water. In Table 2a and b, we consider the ranges of the core radius and shell thickness of TiN nanoshells in which the best geometrical parameters for TiN nanoshells that meet the requirements of long radiative relaxation times, high absorption of solar radiation, and thin shell thicknesses can be realized. It is evident from Table 2a and b that, for TiN nanoshells in air and water, IQ_{abs} reaches its maximum at a particular value of the shell thickness, whereas τ_{rad} increases as the shell thickness is reduced according to eqn (9). On the other hand, as the radius of TiN nanospheres increases, τ_{rad} continually decreases. In the case of TiN nanoshells and nanospheres, τ_{rad} is less than τ_{th} in most cases except for TiN nanoshells embedded in water when R_c = 30–50 nm and d/R_c = 0.05. Additionally, a trade-off is demonstrated between realizing a longer radiative relaxation time and achieving high absorption FoM IQ_{abs}. Overall, compared to TiN nanospheres, TiN nanoshells exhibit significantly longer radiative relaxation times τ_{rad} at the same values of IQ_{abs} or significantly higher IQ_{abs} values at the same values of τ_{rad}.

Assuming an average hot electron energy of $E_h = \epsilon_f + (1/2)\hbar\omega_{sp}$ where $\epsilon_f = \left(\hbar^2/2m_e^*\right)\left(3\pi^2 n_e\right)^{2/3}$ is the Fermi energy, the transit distance of hot electrons in the TiN region during the thermalization time τ_{th} is approximately $\ell \sim \sqrt{2E_h/m_e^*}\tau_{th}$. Since $K_BT \ll \hbar\omega_{sp}$ even at the highest maximum absorption IQ_{abs} of nanoshells where T is the temperature of the particle after illumination, we neglect the variation in the energy of electrons due to the temperature increase of the particle. In light of this, it is necessary to take into account the demand that the shell thickness be less than to the transit distance ℓ of the hot electrons during a time $t < \tau_{th}$. When the size of the TiN shell is less than ℓ, the LSPR will be more concentrated in the TiN region and can be exploited to generate hot electrons that are able to feasibly reach the attached active semiconductor. Additional essential issues, such as the radiative damping of LSPR and the mobility fluctuation of charge carriers, related to the LSPR field spreading over a sizable inactive region inside the particle, can be resolved. In the range of n_e = (1.6–6.6) × 10^{22} cm^{-3} where $m_e^* = (1.7-3.1)m_e$[56] and assuming τ_{th} = 0.15 ps,[69] one finds ℓ = (40–45) nm. As the effective lifetime of hot electrons should be shorter than the thermalization time τ_{th}, the minimum possible shell thickness d is chosen so that $d < \ell$ keeping an eye on the absorption efficiency. However, in this study, the optimal thicknesses of the TiN shell will not be greater than 10 nm.

Based on the above-mentioned discussion and analysis, one can recognize the criteria of the developed TiN nanoshells for hot-electron-related applications. These criteria for optimal TiN nanoshell performance are built upon the geometrical optimization for maximum solar energy absorption, which are as follows: (i) the IQ_{abs} of the nanoshells is greater than the maximum of IQ_{abs} of TiN nanospheres as a reference of performance in this study; (ii) τ_{rad} is as long as possible; and (iii) the shell thickness d is as minimal as possible such that $d < \ell$. From Table 2a and b, one can find optimal design parameters complying to these three criteria, *i.e.*, the numbers in bold in Table 2a and b correspond to the optimal design parameters for the plasmonic systems. For hollow TiN nanoshells in air, the first and second sets are (R_c, d) = (60 nm, 6 nm) and (70 nm, 7 nm) (*i.e.*, d/R_c = 0.1 in both sets), respectively. For hollow TiN nanoshells in water, the first and second sets are (R_c, d) = (40 nm, 8 nm) and (50 nm, 10 nm) (*i.e.*, d/R_c = 0.2 in both sets), respectively. Based on the requirement that the TiN region size should be less than ℓ, it is evident that employing TiN nanoshells is preferable to using TiN nanospheres, whose core radius is usually greater than ℓ for acceptable values of IQ_{abs}. However, in the case of TiN nanoshells which exhibit longer radiation relaxation times τ_{rad} at thin shell thicknesses, $\tau_{rad} < \tau_{th}$ by one order of magnitude as we limit ourselves by the three conditions described above. The improvement in τ_{rad} to be longer will be correlated with a drop in IQ_{abs}. For instance, for TiN nanoshells embedded in water, τ_{rad} = 0.172 ps which is longer than τ_{th} when (R_c, d) = (40 nm, 2 nm) (*i.e.*, d/R_c = 0.05) and IQ_{abs} = 1074 W m^{-2} which is approximately smaller than the best value of IQ_{abs} of TiN nanospheres (2470 W m^{-2}) by a factor of 0.4.

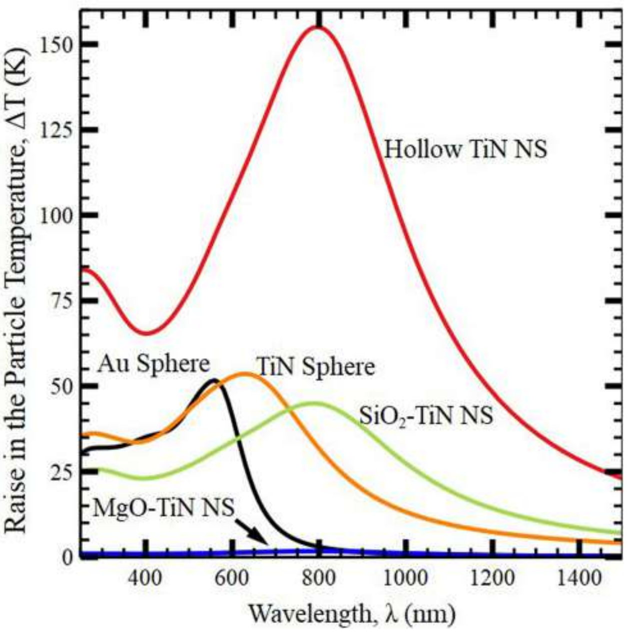

Fig. 6 The increase in the steady state temperature ΔT of Au and TiN nanospheres and hollow TiN, SiO_2–TiN, and MgO–TiN nanoshells in water. The geometrical parameters of these structures are chosen at the highest maximum of IQ_{abs} of the assumed nanostructures, as given in Table 1a and b.

The FoM of solar energy absorption IQ_{abs} quantifies the amount of absorbed solar energy regardless of the effectiveness of generated hot electrons. Indeed, as IQ_{abs} increases, the temperature of NPs will increase. Now, let us examine whether the hot electron dynamics would be affected significantly by the temperature increase of NPs. In Fig. 6, we illustrate the steady state temperature change ΔT calculated using eqn (4) at the highest maximum of $IQ_{abs}(IQ_{abs}^{H\text{-}max})$ for hollow TiN, SiO_2–TiN, and MgO–TiN nanoshells relative to Au and TiN nanospheres in water. The geometrical parameters of all these structures are given in Table 1a and b. To calculate ΔT given by eqn (4), we assume the illumination intensity I = 1 mW μm^{-2} that corresponds to a laser power of 12.5 mW and a laser spot diameter of 4 μm. In the TiN nanoshells, the surface plasmons are mainly stimulated in the TiN region in which heat flows so fast, and then heat diffuses away through the host medium and core. Therefore, in eqn (4), κ_{med} in the case of homogenous spherical particles represents the thermal conductivity of the host medium, while κ_{med} represents the average thermal conductivity of the host medium and core material in the case of nanoshells. Fig. 6 demonstrates that as hollow TiN nanoshells are characterized by the highest $\mathrm{IQ}_{\mathrm{abs}}$, compared to other structures, these nanoshells exhibit the highest temperature increase ΔT. However, the maximum of temperature increase ΔT_{max}, which corresponds to a thermal energy of approximately 0.01 eV, is far smaller than the energy of hot electrons E_{h} (E_{h} is approximately 2 eV for hollow TiN structures). Consequently, the dynamics of the hot electrons will not be significantly affected by the temperature rise in hollow TiN structures. As shown in Fig. 6, the utilization of MgO with a high thermal conductivity as the core of MgO–TiN nanoshells considerably reduces particle heating. Comparing hollow TiN nanoshells to other studied nanoshells and nanospheres, Fig. 6 shows that these nanoshells have the highest NP temperature increase, *i.e.*, the ΔT_{max} of hollow TiN nanoshells is approximately three times higher than those of the other nanostructures. This notable temperature increase of hollow TiN nanoshells is mainly attributed to the observation shown in Fig. 4 and discussed therein, that is, an enhanced level of Q_{abs} of hollow TiN nanoshells can be achieved at relatively smaller TiN shell thicknesses (R_{c} = 50 nm and d = 15 nm). Therefore, for hollow TiN nanoshells, the equivalent radius R_{eq} in the denominator of eqn (4) is comparatively smaller than that of the other particles, leading to effective heat diffusion and a larger temperature increase inside the TiN shell. In addition to the efficiency of using hollow TiN nanoshells for enhancing hot electron generation, this study also reveals that hollow TiN nanoshells are promising nanostructures for efficient light-to-heat conversion applications such as photochemistry, photodetection, and solar thermal energy conversion.

Here, we investigate the local field distribution inside and outside the NP models, TiN nanoshells and TiN and Au nanospheres, demonstrating that the TiN nanoshell structure can offer a higher concentration of LSPR fields in a compact volume of TiN, improving the efficiency of generating hot electrons.[71] In Fig. 7a–c, we plot the distribution of the normalized field intensity of parallel electric fields $|E(r)/E_0|^2$ along the radial direction r for hollow TiN, $\mathrm{SiO_2}$–TiN, and MgO–TiN nanoshells in air and water (Fig. 7a and b, respectively) and for Au and TiN

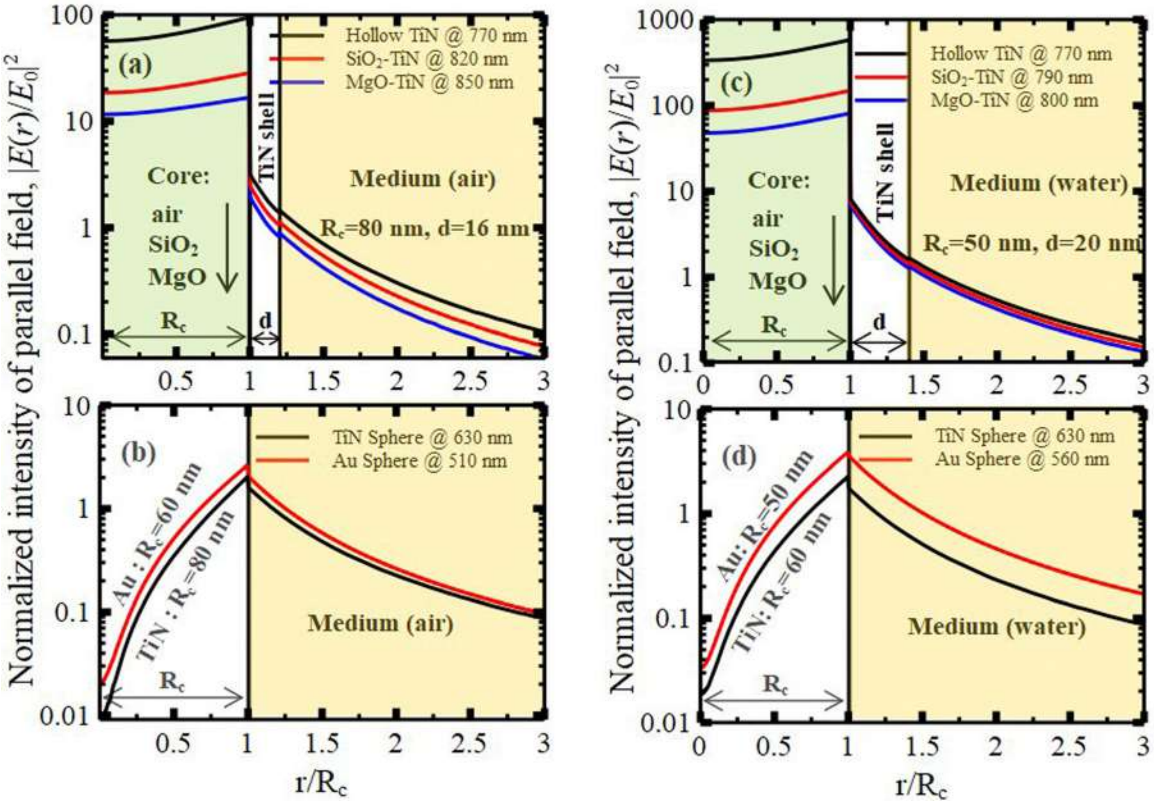

Fig. 7 The radial distribution of the normalized intensity of parallel electric fields $|E(r)/E_0|^2$ for hollow TiN, $\mathrm{SiO_2}$–TiN, and MgO–TiN nanoshells in air (a) and water (b) and for Au and TiN nanospheres in air (c) and water (d). For both structures, we select the structural geometrical parameters at which $\mathrm{IQ}_{\mathrm{abs}}$ exhibits the best maximum value. The electric fields are assumed to be operated at the resonance wavelength of the absorption coefficient Q_{abs}.

nanospheres in air and water (Fig. 7c and d, respectively). The optical field parallel to the polarized incident field is computed assuming $\theta = \pi/2$ in Fig. 1. The perpendicular fields at $\theta = 0$ are insignificant in our structures. For all structures assumed in Fig. 7, we choose the geometrical parameters of the structure where the highest maximum value of IQ_{abs} is attained. The electric fields are calculated at the resonance wavelength of the absorption coefficient Q_{abs}. From Fig. 7a–c, it is observed that the normalized field intensity $|E(r)/E_0|^2$ of hollow TiN nanoshells in the TiN shell region is higher than those of SiO_2–TiN and MgO–TiN nanoshells. Considering the same size of TiN region of 16 nm and 20 nm in air and water, respectively, the average of $|E(r)/E_0|^2$ of the hollow TiN nanoshells is higher than those of Au and TiN nanospheres. The $|E(r)/E_0|^2$ of the hollow TiN nanoshells drops from $\sim$3.1 and $\sim$8.2 at the core–shell surface to $\sim$1.42 and $\sim$1.44 at the shell–medium surface in air and water, respectively. For the same size of TiN region of 16 nm and 20 nm in air and water, $|E(r)/E_0|^2$ in the Au core region of the Au nanosphere drops from $\sim$2.06 and $\sim$3.56 at the core–medium surface to $\sim$0.98 and $\sim$1.23 in air and water, respectively. In the TiN core region of the TiN nanospheres, $|E(r)/E_0|^2$ drops from $\sim$1.6 and $\sim$1.76 at the core–medium surface to $\sim$0.92 and $\sim$0.78 in air and water, respectively. Based on this, it can be concluded that the hollow TiN nanoshells concentrate the LSPR field in a very small region compared to the nanospheres. The highly confined LSPR field in a small volume can be sustained for a longer time, where it is less affected by the radiative damping effect associated with the energy loss of the oscillating electrons in the form of spontaneous emission. Also, in such small volume-sized LSPRs, the fluctuation in carrier density is insignificant due to the insignificant fluctuation in carrier density, and then enhances the swift mobility of generated electrons to reach the operative surface in photocatalysis and solar cell systems.

It is important to note that, despite the high FoM of solar energy absorption of TiN nanoshells relative to that of Au nanoshells, as shown in Fig. 2c and d, their field intensity enhancement is lower than that of Au nanoshells. Therefore, the superiority of incident photon-to-current efficiency (IPCE) of the TiN–semiconductor system over an Au–semiconductor system observed in experiments[15] can be attributed to the longer radiative relaxation time of TiN nanospheres compared to that of Au nanospheres. For instance, in the cases in which the highest maximum IQ_{abs} is achieved, τ_{rad} = 1.59 fs when R_c = 80 nm and τ_{rad} = 1.81 fs when R_c = 60 nm for TiN nanospheres embedded in air and water as provided in Table 2a and b, respectively. In the cases of Au nanospheres embedded in air and water, τ_{rad} = 0.18 fs when R_c = 60 nm and τ_{rad} = 0.39 fs when R_c = 50 nm. To calculate τ_{rad} for Au using eqn (9), we assumed the plasma frequency energy to be 9.06 eV and $m_e^* = 0.99m_e$.[54] It is shown that even though the size of Au nanospheres is smaller than that of TiN nanospheres, the τ_{rad} of Au nanospheres is almost one order of magnitude smaller than that of TiN nanospheres, which leads to a deterioration in the effectiveness of utilization of generated hot electrons. This demonstrates the significance of our main objective in this work, which is to minimize radiative damping on an equal footing of maximizing solar energy absorption through adopting core–shell systems rather than homogenous NP systems.

4. Conclusion

In this work, we demonstrate that TiN nanoshells with a non-absorbing dielectric core can be utilized as an improved energy conversion component in S–M HNPs, with higher geometrical optimization flexibility, wider absorption range tuneability, and effective hot electron generation and utilization ability. Due to the reduced plasmonic-shell dimension, TiN nanoshells provide an effective approach to plasmon-driven hot electron generation and utilization for enhanced photocatalysis and photovoltaic applications. Relative to homogenous plasmonic nanospheres (Au, Ag, and TiN), these TiN nanoshells can be designed to concurrently satisfy the criteria for optimized plasmonic-assisted hot-electron generation, which are (i) a greater FoM for energy absorption, (ii) a longer radiative damping relaxation time, and (iii) a convenient reduced shell thickness shorter than the possible hot electron survival distance. In addition, among the three investigated core materials (air, SiO_2, and MgO), hollow-TiN nanoshells showed a promising and better functionality.

For systematic studies, we initially optimize the geometrical parameters of all NP models (nanosphere and nanoshell models) to achieve the maximum FoM of solar energy absorption. It is demonstrated that TiN nanoshells absorb solar energy more efficiently than TiN and noble metal nanospheres. Among the proposed TiN nanoshells with a core of air, SiO_2, and MgO, the hollow TiN nanoshells with the lowest possible studied dielectric constant show the highest solar energy absorption. Next, we carefully examine the effect of other crucial factors on the generation and transport of hot electrons including the radiative damping, the plasmon field features, and the temperature increase of the NPs.

Investigating the optical field features of TiN nanoshells and TiN nanospheres, it is shown that the plasmon field intensity of hollow TiN nanoshells is highest and most concentrated in a smaller volume of TiN. We further clarify that, despite the high solar absorption realized by hollow nanoshells, the associated temperature rise of these nanoshells has no discernible impact on their performance. In light of the temporal dynamics of hot electrons, it is demonstrated that employing hollow TiN nanoshells with thin shells significantly resolves the issues that restrict the amount of charge carriers that reach the attached photocatalyst semiconductor. The reduction in the shell thickness enhances the localization of the plasmon field intensity and suppresses the radiative damping effects while leading to a deterioration of the efficiency of solar energy absorption. Therefore, the eventual optimal structural parameters of optimized hollow nanoshells must take into account the tradeoff between all factors that control the creation and extraction of hot electrons.

Author contributions

S. Moustafa: conceptualization, investigation, methodology, data curation, validation, formal analysis, writing – original draft preparation, writing – review and editing. M. K. Zayed: conceptualization, investigation, methodology, data curation, validation, formal analysis, writing – original draft preparation, writing – review and editing. K. O. Daffallah: methodology, data curation, validation, formal analysis. N. M. Shaalan: methodology, data curation, validation, formal analysis. M. Rashad: methodology, data curation, validation, formal analysis. H. Fares: conceptualization, investigation, methodology, data curation, validation, formal analysis, writing – original draft preparation, writing – review and editing.

Data availability

The data that support the findings of this study are available from the corresponding author [H. Fares] upon reasonable request.

Conflicts of interest

The authors have no conflicts to disclose.

References

1 S. Chen, D. Huang, P. Xu, W. Xue, L. Lei, M. Cheng, R. Wang, X. Liu and R. Deng, *J. Mater. Chem. A*, 2020, **8**, 2286–2322.

2 M. R. Hoffmann, S. T. Martin, W. Choi and D. W. Bahnemann, *Chem. Rev.*, 1995, **95**, 69–96.

3 F. Hamidi and F. Aslani, *Nanomaterials*, 2019, **9**, 1444–1476.

4 A. Fujishima, T. N. Rao and D. A. Tryk, *J. Photochem. Photobiol., C*, 2000, **1**, 1–21.

5 Y. Ben-Shahar and U. Banin, *Top. Curr. Chem.*, 2016, **374**, 54–79.

6 L. Sang, Y. Zhao and C. Burda, *Chem. Rev.*, 2014, **114**, 9283–9318.

7 M. S. Arshad, S. Trafela, K. Z. Rožman, J. Kovac, P. Djinovic and A. Pintar, *J. Mater. Chem.*, 2017, **5**, 10509–10516.

8 A. Fujishima and K. Honda, *Nature*, 1972, **238**, 37–38.

9 T. Wang, Z. Luo, C. Li and J. Gong, *Chem. Soc. Rev.*, 2014, **43**, 7469–7484.

10 M. W. Knight, L. Liu, Y. Wang, L. Brown, S. Mukherjee, N. S. King, H. O. Everitt, P. Nordlander and N. J. Halas, *Nano Lett.*, 2012, **12**, 6000–6004.

11 M. Lee, J. U. Kim, K. J. Lee, S. Ahn, Y. Shin, J. Shin and C. B. Park, *ACS Nano*, 2015, **9**, 6206–6213.

12 A. D. Phan, N. B. Le, N. T. H. Lien and K. Wakabayashi, *J. Phys. Chem. C*, 2018, **122**, 19801–19806.

13 B. Doiron, M. Mota, M. P. Wells, R. Bower, A. Mihai, Y. Li, L. F. Cohen, N. M. Alford, P. K. Petrov, R. F. Oulton and S. A. Maier, *ACS Photonics*, 2019, **6**, 240–259.

14 T. Liu, Q. W. C. Zhang, X. Li and J. Hu, *arXiv*, 2017, preprint, arXiv:2107.08258, arxiv.org/abs/2107.08258.

15 A. Naldoni, U. Guler, Z. Wang, M. Marelli, F. Malara, X. Meng, L. V. Besteiro, A. O. Govorov, A. V. Kildishev, A. Boltasseva and V. M. Shalaev, *Adv. Opt. Mater.*, 2017, **5**, 1601031.

16 A. A. Barragan, S. Hanukovich, K. Bozhilov, S. S. R. K. C. Yamijala, B. M. Wong, P. Christopher and L. Mangolini, *J. Phys. Chem. C*, 2019, **123**, 21796–21804.

17 A. A. Barragan, N. V. Ilawe, L. Zhong, B. M. Wong and O. L. Mangolini, *J. Phys. Chem. C*, 2017, **121**, 2316–2322.

18 X. Kan, C. Deng, C. Yu, J. Ding and H. Zhu, *J. Mater. Sci.: Mater. Electron.*, 2018, **29**, 10624–10630.

19 I. V. Zelepukin, A. A. Popov, V. O. Shipunova, G. V. Tikhonowski, A. B. Mirkasymov, E. A. Popova-Kuznetsova, S. M. Klimentov, A. V. Kabashin and S. M. Deyev, *Mater. Sci. Eng., C*, 2021, **120**, 111717.

20 S. Linic, S. Chavez and R. Elias, *Nat. Mater.*, 2021, **20**, 916–924.

21 H. H. Gustafsona, D. H. Casper, D. W. Grainger and H. Ghandehari, *Nano Today*, 2015, **10**, 67–80.

22 W. Li, A. Elzatahry, D. Aldhayan and D. Zhao, *Chem. Soc. Rev.*, 2018, **47**, 8203–8237.

23 H. Li, Y. He, Z. Liu, B. Jiang and Y. Huang, *Sol. Energy Mater. Sol. Cells*, 2017, **166**, 52–60.

24 W. Lv, P. E. Phelan, R. Swaminathan, T. P. Otanicar and R. A. Taylor, *J. Sol. Energy Eng.*, 2013, **135**, 021004–021010.

25 M. Chen, Y. He, X. Wang and Y. Hu, *Appl. Energy*, 2018, **211**, 735–742.

26 H. Minassian, K. Madoyan and A. Melikyan, *Plasmonics*, 2012, **7**, 745–748.

27 H. Fares, M. Ahmed and S. Moustafa, *Phys. Scr.*, 2023, **98**, 035509–035522.

28 A. Manjavacas, J. G. Liu, V. Kulkarni and P. Nordlander, *ACS Nano*, 2014, **8**, 7630–7638.

29 D. Rativa and L. A. Gómez-Malagón, *Renewable Energy*, 2018, **118**, 947–954.

30 J. Q. M. Almarashi, S. Moustafa, M. Ahmed and H. Fares, *NANO*, 2023, **18**, 2350068.

31 Y. Zou, X. Li, L. Yang, B. Zhang and X. Wu, *Int. J. Therm. Sci.*, 2023, **185**, 108099.

32 K. Kadoya, N. Matsunaga and A. Nagashima, *J. Phys. Chem. Ref. Data*, 1985, **14**, 947–970.

33 R. W. Powee, C. Y. Ho and P. E. Liley, NSRDS-NBS, 1966, 8, Category 5.

34 Y. S. Touloukian, R. W. Powell, C. Y. Ho and P. G. Klemens, *Thermo- physical Properties of Matter*, IFI/Plenum, New York, 1970, vol. 2.

35 T. D. Lee and A. U. Ebong, *Renewable Sustainable Energy Rev.*, 2017, **70**, 1286–1297.

36 F. Bella, C. Gerbaldi, C. Barolo and M. Grätzel, *Chem. Soc. Rev.*, 2015, **44**, 3431–3473.

37 T. Hisatomi, J. Kubotaa and K. Domen, *Chem. Soc. Rev.*, 2014, **43**, 7520–7535.

38 U. Mahajan, M. Dhonde, K. Sahu, P. Ghosh and P. M. Shirage, *Mater. Adv.*, 2024, **5**, 846–895.

39 Z. Li, J. Zhang, B. Y. Guan and X. W. D. Lou, *Angew. Chem., Int. Ed.*, 2017, **56**, 16003–16007.

40 J. Chen, X. Wei, J. Zhang, Y. Luo, Y. Chen, G. Wang and R. Wang, *Ind. Eng. Chem. Res.*, 2019, **58**, 2741–2748.

41 A. L. Aden and M. Kerker, *J. Appl. Phys.*, 1951, **22**, 1242–1246.

42 M. Kerker, *The Scattering of Light and Other Electromagnetic Radiation*, Academic, New York, 1969.

43 G. Mie, *Ann. Phys.*, 1908, **330**, 377–624.

44 O. B. Toon and T. P. Ackerman, *Appl. Opt.*, 1981, **20**, 3657–3660.

45 M. Kumar, N. Umezawa, S. Ishii and T. Nagao, *ACS Photonics*, 2016, **3**, 43–50.

46 S. Moustafa, M. K. Zayed, M. Ahmedd and H. Fares, *Phys. Chem. Chem. Phys.*, 2024, **26**, 1994–2006.

47 D. P. Tsai and T. Tanaka, *Proc. SPIE*, 2017, 10346.

48 S. Link and M. A. El-Sayed, *Int. Rev. Phys. Chem.*, 2000, **19**, 409–453.

49 G. Baffou and R. Quidant, *Laser Photonics Rev.*, 2012, **7**, 1–17.

50 C. F. Bohren and D. R. Huffman, *Absorption and Scattering of Light by Small Particles*, Wiley-VCH Verlag GmbH, Weinheim, Germany, 1998.

51 G. Baffou, P. Berto, E. B. Ureña, R. Quidant, S. Monneret, J. Polleux and H. Rigneault, *ACS Nano*, 2013, **7**, 6478–6488.

52 H. Hövel, S. Fritz, A. Hilger, U. Kreibig and M. Vollmer, *Phys. Rev.*, 1993, **48**, 18178–18188.

53 S. M. Edlou, J. C. Simons, G. A. Al-Jumaily and N. A. Raouf, *Proc. SPIE*, 1994, **2262**, 96–106.

54 P. B. Johnson and R. W. Christy, *Phys. Rev. B: Condens. Matter Mater. Phys.*, 1972, **6**, 4370–4379.

55 P. Patsalas, N. Kalfagiannis and S. Kassavetis, *Materials*, 2015, **8**, 3128–3154.

56 C. G. H. Walker, J. A. D. Matthew, C. A. Anderson and N. M. D. Brown, *Surf. Sci.*, 1998, **412/413**, 405–414.

57 P. Patsalas and S. Logothetidis, *J. Appl. Phys.*, 2001, **90**, 4725–4734.

58 A. D. Rakić, A. B. Djurišić, J. M. Elazar and M. L. Majewski, *Appl. Opt.*, 1998, **37**, 5271–5283.

59 N. W. Ashcroft and N. D. Mermin, *Solid State Physics*, Saunders Collage Publishing, 1976.

60 I. H. Malitson, *J. Opt. Soc. Am.*, 1965, **55**, 1205–1209.

61 R. E. Stephens and I. H. Malitson, *J. Res. Natl. Bur. Stand.*, 1952, **49**, 249–252.

62 C. J. Murphy, A. M. Gole, S. E. Hunyadi, J. W. Stone, P. N. Sisco, A. Alkilany, B. E. Kinard and P. Hankins, *Chem. Commun.*, 2008, 544–557.

63 K. Laaksonen, S. Suomela, S. R. Puisto, N. K. J. Rostedt, T. Ala-Nissila and R. M. Nieminen, *J. Opt. Soc. Am. B*, 2014, **31**, 494–502.

64 E. A. Chaffin, S. Bhana, R. T. O'Connor, X. H. Huang and Y. M. Wang, *J. Phys. Chem. B*, 2014, **118**, 14076–14084.

65 E. Prodan, P. Nordlander and N. J. Halas, *Nano Lett.*, 2003, **3**, 1411–1415.

66 B. Doiron, Y. Li, A. Mihai, S. D. Forno, S. Fearn, L. F. Cohen, N. M. Alford, J. Lischner, P. Petrov, S. A. Maier and R. F. Oulton, *ACS Appl. Mater. Interfaces*, 2023, **15**, 30417–30426.

67 B. Doiron, Y. Li, A. Mihai, R. Bower, N. M. Alford, P. K. Petrov, S. A. Maier and R. F. Oulton, *J. Phys. Chem. C*, 2019, **123**, 18521–18527.

68 S. I. Anisimov, B. L. Kapeliovich and T. L. Perelman, *J. Exp. Theor. Phys.*, 1976, **39**, 375–377.

69 S. D. Forno and J. Lischner, *Phys. Rev. Mater.*, 2019, **3**, 115203.

70 A. Melikyan and H. Minassian, *Appl. Phys. B: Lasers Opt.*, 2004, **78**, 453–455.

71 S. Moustafa, J. Q. M. Almarashi, M. Almokhtar, H. Fares and M. K. Zayed, *Appl. Phys. A: Mater. Sci. Process.*, 2023, **129**, 376–387.